# <arttitle> Three-dimensional mapping of a deformation field inside a nanocrystal

<aug> Mark A. Pfeifer, Garth J. Williams, Ivan A. Vartanyants, Ross Harder &  Ian K. Robinson

*<aff> Physics Dept., University of Illinois, Urbana IL 61801, USA*

<footnote> Present addresses: Dept. of Physics, Univ. of  Oregon, Eugene, OR 97403, USA (MAP), School of Physics, Univ. Melbourne, Australia (GJW), HASYLAB, DESY, Hamburg, Germany (IAV), Dept of Physics and Astronomy, University College, London, UK (IKR).

**<abs> Contact forces are inevitable whenever nanocrystals are prepared on a substrate and these must result in strain fields within the crystals which are relevant to their epitaxy[1]. Coherent X-ray diffraction patterns, measured using the latest third-generation synchrotron radiation sources, can be inverted to obtain full 3D images of the interior density within such nanocrystals[2,3,4].  Diffraction from an ideal crystal lattice results in an identical copy of this continuous diffraction pattern at every Bragg peak.   When strain is present, the copies are no longer identical and contain additional information, appearing as broken local inversion symmetry about each Bragg point.  Here we show that one such pattern can be inverted nevertheless to obtain a *complex* crystal density, whose phase encodes a projection of the lattice deformation.  A lead nanocrystal was crystallized in ultra-high vacuum from a droplet on a silica substrate and equilibrated close to its melting point.  A 3D image of the density, obtained by inversion of the coherent X-ray diffraction, shows the expected facetted morphology, but in addition reveals a real-space phase that is consistent with the 3D evolution of a deformation field arising from interfacial contact forces. Quantitative 3D imaging of lattice strain on the nanometre scale will have**

**profound consequences for our fundamental understanding of grain interactions and defects in crystalline materials[1]. Our method of measuring and inverting diffraction patterns from nanocrystals represents a vital step towards the ultimate goal of atomic resolution single-molecule imaging that is a prominent justification for development of X-ray free-electron lasers[5,6,7].**

<p> Coherent X-ray diffraction imaging is a rapidly advancing form of microscopy that was opened up by the realisation that oversampled diffraction patterns can be inverted to obtain real-space images. The possibility was first pointed out by Sayre[2] but not demonstrated until 1999 by Miao et al[3]. The phase information of the diffraction pattern, which is lost in its recording, is embedded in a sufficiently oversampled diffraction pattern because this is intimately related to the Fourier transform of the object under investigation. The inversion of diffraction back to an image has been proven to be unique in two or higher dimensions, except for 'pathological' cases of internal symmetry of the object or its diffraction pattern[8,9]. Computational methods of performing the inversion are an active area of development; they are often based on the iterative Hybrid Input-Output (HIO) method introduced in the 1980's by Fienup[10].

<p> Lensless imaging using coherent X-rays is an attractive alternative to electron microscopy because of better penetration of the electromagnetic waves in materials of interest; multiple scattering effects can be neglected so the first Born approximation can be safely used. In some cases X-rays are less damaging to the sample than electrons and, in either case, the collection of a diffraction pattern is inherently more efficient than the use of lenses[11]. If the diffraction can be reliably inverted by computation, the method could be routinely used to reveal the structure of materials on the nanometre scale, far beyond the resolution of the traditional light microscope. The holographic method of combining a reference wave is an alternative way to perform the inversion[12].

<p> The use of short-wavelength X-rays and crystalline materials introduces the additional possibility of Bragg diffraction. In the simplest approximation of ideal crystals, this yields an identical copy of the forward diffraction centred around each Bragg peak. Using Bragg diffraction patterns not only allows individual grains to be selected for analysis one-by-one and avoids losing data behind a beam-stop[3], but also greatly facilitates the recording in three dimensions (3D), as demonstrated for micron-sized gold crystals[4]. The inversion is formally identical to that of the forward scattering[3], but reveals only the density of the crystalline part of the sample, so is highly sensitive to defects.

<p> Diffraction also opens the new possibility of directly imaging the strain fields within the crystal, an opportunity that is exploited in the current work. It is easy to demonstrate that the presence of strain breaks the local symmetry of a diffraction pattern about the Bragg point, which would otherwise show inversion symmetry (as it does about the origin according to Friedel's law). While the inverse Fourier transform of a symmetric function is real, that of the asymmetric distribution must in general be complex, possessing phase structure in real space. It has been shown[13] that, without loss of generality, the density of a crystal can be considered to be complex function whose magnitude is the physical electron density and whose phase is the projection of the local deformations of the crystal lattice onto the reciprocal lattice vector, $\mathbf{Q}$, of the Bragg peak about which the diffraction is measured.

<p> Since there are twice as many independent measurement points for an asymmetric diffraction pattern than a centrosymmetric one and twice as many variables needed to describe a complex density function as a real one, the problem is overdetermined to the same degree. The oversampling ratio[14], which determines whether such a pattern can be inverted, is the same. The primary measure of the oversampling of the diffraction is the size of the 'support' region that is the volume of

space within which the finite-sized object is confined to exist[14]; this constraint is unchanged for the complex problem. In our experience with test calculations, we have found no additional difficulty in the convergence of the HIO-like algorithms for the complex problem, and this has been confirmed by others[15,16]. The greatest sensitivity arises from the choice of the support constraint, just as it does for the real density problem.

<p> Following our earlier preparation of free-standing Au nanocrystals[4], we developed a method to grow nanometre-sized Pb crystals inside the vacuum chamber of the 34-ID-C beamline at the Advanced Photon Source (APS), shown schematically in Fig 1. X-ray diffraction measurements were then made *in situ* of the continuous diffraction pattern surrounding a (111) Bragg peak. Figs 1 and S2 show slices through the concentric shells of intensity that correspond to the shape transform of the hemispherical crystal. Additionally, a number of flares can seen, which arise from facets formed during solidification of the crystal. Scanning Electron Microscope (SEM) images, also shown in Fig 1, subsequently found the sample to contain an array of isolated crystals with a facetted hemispherical morphology and a distribution of sizes centred around 200nm.

<p> The 3D data were inverted to real space in the coordinate system of the measurement, following the two directions of the CCD's pixel array and the sample rotation angle. Initial attempts to phase the background-subtracted diffraction pattern were made using established methods[4,10,14-17]. We applied as many as 7 alternating cycles of Error Reduction (ER) and Fienup's HIO algorithm, each consisting of many iterations of the respective algortihm[10], with real-valuedness and finite support as the real-space constraints. The support region was allowed to shrink by thresholding the images obtained by prior inversions with a larger support[17]. Despite using a tight support, the recovered density included a large region of low density within the crystal

boundary.  This region featured a non-uniform phase despite constraining the phases to be zero on every iteration.

<p> When we phased the diffraction pattern *without* enforcing a real-space phase constraint, we obtained qualitatively better results.  Fifteen phasing calculations were performed in a 324x192x48 array, comprising 200 iterations of HIO followed by 1000 iterations of ER, each starting with different random starting phases, using a simple 41x37x24 rectangular support with more than twice the volume of the tight support used previously.  All fifteen results had an error metric, defined as the normalized integrated squared difference between the Fourier transform of the image and the data, between 0.022 and 0.023.  When the results with the three lowest error metrics were compared, they showed a reproducibility of 0.024 (analogous definition), meaning that, within the accuracy of the data, they were identical[18].  The magnitude of the complex density (Fig S4) is then assumed to be the physical density, while the phase (Figs 3 and S5) is interpreted as the scalar product of the local deformation and the momentum transfer vector[13], $\mathbf{Q}$.  A geometric calculation was then used to transform the result to orthogonal directions in real space[19] for viewing the image in a Cartesian laboratory frame (Figs 2 and S3).  These images showed a relatively uniform internal density, varying about 15%, with a phase gradient where the density had been weaker before.

<p> The physical density map in Fig S4 showed the crystal shape to be a sphere of diameter 750nm with flat facets, as expected[20] for the equilibrium crystal shape of Pb, due to anisotropy of its surface free energy[21], $\gamma$.  Angular variations of $\gamma$ cause facetting along certain crystallographic directions through the Wulff construction[21].  A least-squares fit to the density boundary of our sample, shown in Figs 2 and S6, identified clear facets along {111} directions as well as the plane of the interface with the substrate, which was non-crystallographic[19].  To estimate the resolution of the final image, we plotted line scans of the density projected onto the normals of these facets, as

well as radial scans through the spherical regions in Fig S7. These illustrate how steeply the density edge of the crystal drops across the boundary of the crystal. The density step could be well-described in Fig S7 by fitting error functions of width 40nm, which was taken to be the image resolution.

<p> The main focus of our attention is the internal strain fields revealed by the phase of the complex density in Figs 3 and S5. Most of the crystal was undeformed, with a constant phase, but significant deviations appeared in an egg-shaped bulge near the middle of its interface with the substrate, rising to a maximum of 1.1 radians at the bottom edge of the crystal where it makes contact with the substrate. This corresponds to a maximum deformation of the crystal of $(1.1/2\pi)$ (111) lattice spacings, or 0.5Å. The phase bulge is illustrated in Fig 4a as an isosurface of constant phase and as contour plots of a 2D slice through the phase map in Fig 4c. Across the short direction of the bulge, the equal-phase contours are seen to have a roughly circular shape. This is consistent with the radial deformation field **u(r)** of a classical point defect, such as a lattice interstital or vacancy. When such a deformation field is projected onto the **Q**-vector, the resulting phase forms two spheres (of constant **Q·u(r))** which touch at the location of the defect[22]. In our image, only part of a sphere is seen, indicating the point defect is virtual, lying outside the crystal. To simulate the long direction of the phase bulge, we constructed a model that superimposes two lines of point defects of opposite sign. The full calculated phase isosurface from the resulting deformation is shown in Fig 4b. This model explains both the detailed shape of the phase contours and the inverse-square variation of the strain projection with distance, consistent with the observed spacing of the contours in Fig 4c.

<p> The point defects assumed to explain the data are virtual sources of the deformation field, lying outside the crystal. The physical origin of this strain is a surface deformation distributed across the interface with the $SiO_2$ substrate. The surface

distortion results in a long-range strain field within the crystal, exactly analogous to the effect of surface charges in electrostatics. It is likely that the Pb crystal had nucleated from the melt at some surface defect of the substrate that imparts a residual contact strain. The surface strain distribution is connected with the measured deformation distribution by the Poisson equation governing continuum elasticity theory.

<p> Our result shows that physically reasonable strain fields can be imaged three-dimensionally inside crystalline materials of nanometre dimensions. The deformation field seen in our Pb nanocrystal is attributed to a surface defect on the substrate where the crystal nucleated. It is clear that, by extension of this work, all of the classic defects, the basic ingredients of materials science, could be imaged in this way. The use of a nanocrystal host limits the volume of space that has to be mapped to see an isolated defect, but also serves as the support needed for the diffraction phasing to succeed. Our method of obtaining phase contrast is naturally complimentary to the real-space strain-mapping methods that depend on the preparation of nanometre-sized beams[23], and to the Fresnel zone-plate-based methods[24]. Our resolution is presently 40nm, but can be improved substantially by the development of better detectors and optics or more powerful and more coherent x-ray sources, such as an X-ray free-electron laser[6]. The 3D imaging of complete nanocrystals, using the inversion methods demonstrated here, will naturally extend to atomic resolution when such measurements become possible[5,7].

&lt;bibcit&gt; 1. Cahn R.W., Epitaxy keeps rolling along. Nature 375, 363-364 (1995)

&lt;bibcit&gt; 2. D. Sayre, Some Implications of a theorem due to Shannon. Acta Cryst. 5, 843 (1952)

&lt;bibcit&gt; 3. Miao, J., Charalambous, P., Kirz, J. & Sayre, D., Extending the methodology of X-ray crystallography to allow imaging of micrometre-sized non-crystalline specimens, Nature 400 342-344 (1999)

&lt;bibcit&gt; 4. Williams, G. J., Pfeifer, M. A., Vartanyants, I. A. & Robinson, I. K. Three-dimensional Imaging of Microstructure in Gold Nanocrystals, Phys. Rev. Letters 90 175501-1 (2003)

&lt;bibcit&gt; 5. Neutze R., Wouts R., van der Spoel D., Weckert E. & Hajdu J, Potential for biomolecular imaging with femtosecond X-ray pulses, Nature 406, 752-757 (2000)

&lt;bibcit&gt; 6. Patel, N., Shorter, brighter, better. Nature 415, 110-111 (2002)

&lt;bibcit&gt; 7. Huldt, G., Szöke, A. & Hajdu, J., Diffraction imaging of single particles and biomolecules. J. Struct. Biol. 144, 219-227, (2003).

&lt;bibcit&gt; 8. Bates, R.H.T., Fourier phase problems are uniquely solvable in more than one dimension. Optik, 61 247-262 (1982)

&lt;bibcit&gt; 9. Hayes, M.H., The Reconstruction of a Multidimensional Sequence from the Phase or Magnitude of its Fourier Transform, IEEE Trans. on Acoustics Speech and Signal Processing, 30 140-154 (1982)

&lt;bibcit&gt; 10. Fienup, J. R. Phase retrieval algorithms: a comparison, Appl. Opt. 21, 2758-2769 (1982)

&lt;bibcit&gt; 11. Henderson, R., The Potential and Limitations of Neutrons, Electrons, and X-Rays for Atomic Resolution Microscopy of Unstained Biological Molecules, Quart. Rev. Biophys. 28 171-193 (1995)

&lt;bibcit&gt; 12. Eisebitt, S., Luning, J., Schlotter, W.F., Lorgen, M., Hellwig, O., Eberhardt, W. & Stohr, J. Lensless imaging of magnetic nanostructures by X-ray spectro-holography, Nature 432 885-888 (2004)

&lt;bibcit&gt; 13. Vartanyants, I. A. & Robinson, I. K. Partial Coherence Effects on the Imaging of Small Crystals using Coherent X-ray Diffraction, J. Phys. Condensed Matter 13 10593-611 (2001)

&lt;bibcit&gt; 14. Miao J., Sayre D. & Chapman H.N., Phase retrieval from the magnitude of the Fourier transforms of nonperiodic objects. J. Optical Soc. Amer. A 15 1662-1669 (1998)

&lt;bibcit&gt; 15. Fienup, J.R., Reconstruction of a complex-valued object from the modulus of its Fourier transform using a support constraint, J. Opt. Soc. Amer. A 4 118-123 (1987)

&lt;bibcit&gt; 16. McBride, W., O'Leary, N. L. & Allen, L. J. Retrieval of a Complex-Valued Object from its Diffraction Pattern, Phys. Rev. Letters. 93 233902 (2004)

&lt;bibcit&gt; 17. Marchesini S., He H., Chapman H.N., Hau-Riege S.P., Noy A., Howells M.R., Weierstall U. & Spence J.C.H., X-ray image reconstruction from a diffraction pattern alone, Phys. Rev. B 68 140101 (2003)

&lt;bibcit&gt; 18. Williams, G. J., Pfeifer, M. A., Vartanyants, I. A. & Robinson, I. K. Effectiveness of Iterative Algorithms in Recovering Phase in the Presence of Noise, submitted to Acta Cryst. A (2005)

&lt;bibcit&gt; 19. Pfeifer, M. A., Ph.D. dissertation, University of Illinois (2004)

&lt;bibcit&gt; 20. Heyraud, J. C. & Métois, J. J., Equilibrium Shape and Temperature: Lead on Graphite, Surf. Sci. 128 334-342 (1982)

<bibcit> 21. Wortis, M. Equilibrium crystal shapes and Interfacial phase transitions, *Chemistry and Physics of Solid Surfaces VII*, ed R. Vanselow and R. Howe (Springer Verlag, Berlin, 1988)

<bibcit> 22. Metzger, T. H. & Peisl, H., Huang diffuse x-ray scattering from lattice strains in high-concentration Ta-H alloys. J. Phys F 8 391-402 (1978)

<bibcit> 23. Larson B.C., Yang W., Ice G.E., J. D. Budai, J.D., & Tischler, J.Z. Three-dimensional X-ray structural microscopy with submicrometre resolution. Nature 415 887-890 (2002)

<bibcit> 24. Jacobsen C. & Kirz J., X-ray microscopy with synchrotron radiation, Nature Structural Biology 5 650-653 (1998)

<supp> **Supplementary Information,** including Figures S1 to S7, accompanies the paper on
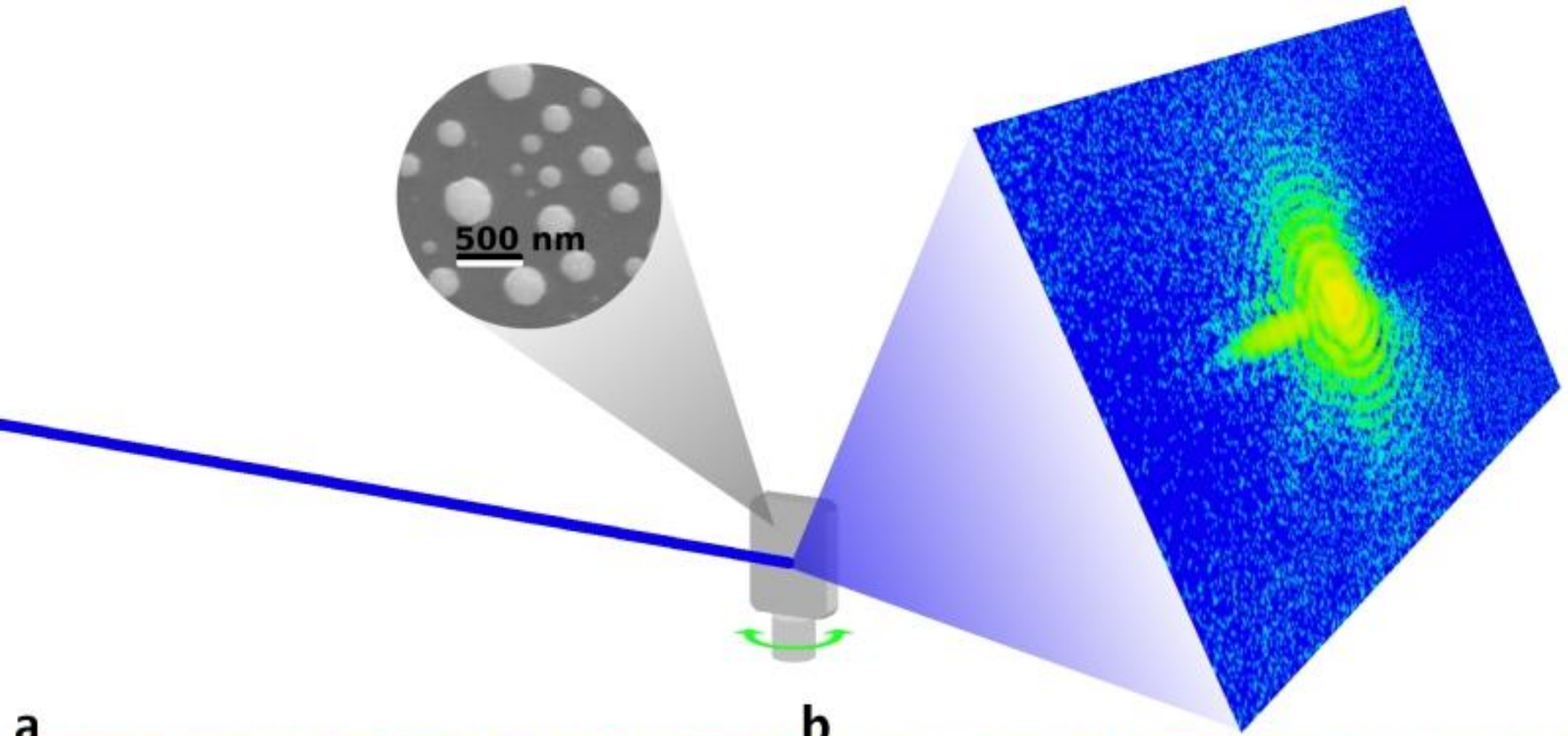
**www.nature.com/nature**.

<corr> Correspondence and requests for materials should be addressed to I.K.R. (i.robinson@ucl.ac.uk).

<LEGEND> Figure 1. Schematic diagram of the coherent X-ray diffraction experiment. Pb was evaporated onto a heated Si wafer support, with its native oxide intact, to make a film of about 20nm thickness. After melting the film, it formed molten droplets, which were then cooled to overcome the (substantial) supercooling until the liquid crystallized, then raised again to 1.2K below the Pb melting point of 600.6K. Ultra-high vacuum (UHV) conditions were maintained throughout. Later examination by SEM (inset) showed isolated hemispherical crystals. Undulator X-rays from the Advanced Photon Source (APS) were monochromated using Si(111), selecting a wavelength of 1.38Å, and collimated by narrow slits to illuminate a few hundred crystals of the sample. A direct-reading CCD X-ray detector, 1.32m away, was centred on the (111) Bragg peak of one of the crystals, to give the diffraction patterns shown. A rotation series of 50 diffraction patterns was collected by rotating the sample in steps of 0.01° about the axis shown. Two representative frames are shown in panels a and b, while a fuller series is given in Fig S2. The total exposure time of each frame was 150s.
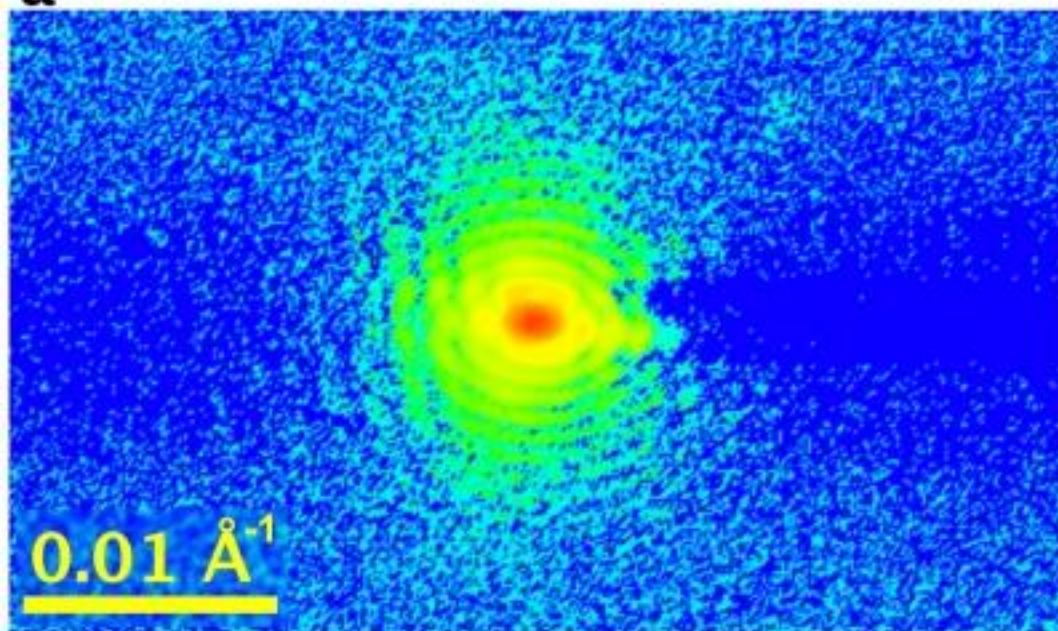
<LEGEND> Figure 2a and c. Two views of the 3D reconstruction of the magnitude of the nanocrystal's complex density function, illustrated as a 50% density isosurface. The fitted facet planes of the equilibrium crystal shape have been coloured. 2b, Schematic fitting model of a sphere (semi-transparent) and facet planes (disks). The diameter of the nanocrystal is 750nm.

<LEGEND> Figure 3. Phase maps cutting through the crystal at three parallel planes shown schematically, separated 138 nm apart. The colour map, labelled in radians, is indicated below. The translucent box is the support region used in the phasing calculations, which was rectangular before the coordinate transformation. The phase bulge is interpreted as a projection of strain fields in the crystal lattice arising from contact forces at the interface with the substrate. Further sections of the phase map are provided in supplementary Figure S5.
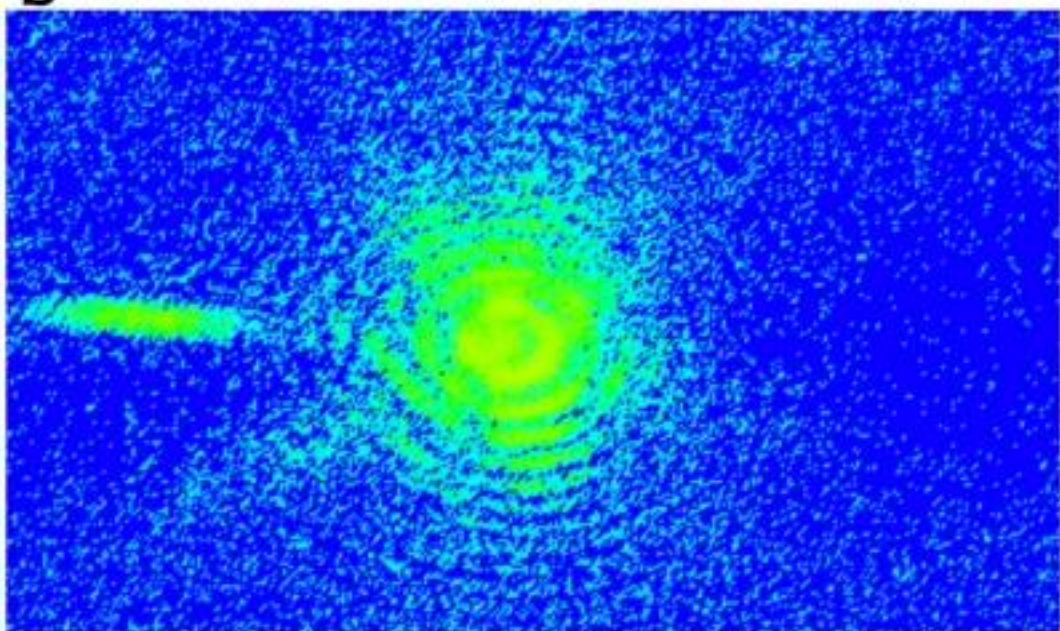
<LEGEND> Figure 4a and b. Single isosurface of the reconstructed phase of the complex density function and its best fit, superimposed on a cut-away image of the crystal density. The point defect lines used to generate the fit (dots) and the direction of **Q** (arrow) are also illustrated. An animated version of this figure is presented in the Supplementary Information as Fig S1. 4c Contour map of the reconstructed phase on a cross-section plane passing near the middle of the nanocrystal in the same view. Smooth lines are the corresponding contours of the projection function **Q·u(r)** where **u(r)** is the strain field calculated for two rows of point defects (balls) of opposite sign. Both sets of contours have spacings of 0.24 radians.

500 nm
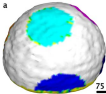
a

0.01 Å⁻¹

b

a      b      c

75 nm

75 nm

-1.6    -0.8    0.0    0.8    1.6